Article

The Solar Radiation Climate of Greece

Harry D. Kambezidis [1,2]

1   Emeritus Researcher, Atmospheric Research Team, Institute of Environmental Research and Sustainable Development, National Observatory of Athens, GR-11810 Athens, Greece; harry@noa.gr
2   Research Associate, Laboratory of Soft Energies and Environmental Protection, Department of Mechanical Engineering, University of West Attica, GR-12241 Athens, Greece

Abstract: The solar radiation climate of Greece is investigated by using typical meteorological years (TMYs) at 43 locations in Greece based on a period of 10 years (2007–2016). These TMYs include hourly values of global, H_g, and diffuse, H_d, horizontal irradiances from which the direct, H_b, horizontal irradiance is estimated. Use of the diffuse fraction, k_d, and the definition of the direct-beam fraction, k_b, is made. Solar maps of annual mean H_g, H_d, k_d, and k_b are prepared over Greece under clear and all skies, which show interesting but explainable patterns. Additionally, the intra-annual and seasonal variabilities of these parameters are presented and regression equations are provided. It is found that H_b has a negative linear relationship with k_d; the same applies to H_g with respect to k_d or with respect to the latitude of the site. It is shown that k_d (k_b) can reflect the scattering (absorption) effects of the atmosphere on solar radiation, and, therefore, this parameter can be used as a scattering (absorption) index. An analysis shows that the influence of solar variability (sunspot cycle) on the H_g levels over Athens in the period 1953–2018 was less dominant than the anthropogenic (air-pollution) footprint that caused the global dimming effect.

Keywords: solar radiation; climate; scattering index; absorption index; Greece

1. Introduction

Solar radiation is the primary source for life on Earth as it controls various fields (atmospheric environment, e.g., [1]; terrestrial ecosystems, e.g., [2]; terrestrial climate, e.g., [3]). Solar radiation is the most abundant renewable energy source; its exploitation started intensively twenty years ago mainly for photovoltaic (PV) installations [4,5]. Fluctuations in the solar radiation intensity are due to changes in the atmospheric constituents [6], variations in the amount and texture of clouds [7], as well as the Sun–Earth geometry variability (Milankovitch theory [8]). Therefore, clouds and atmospheric aerosols are two factors that play a significant role in determining the solar radiation climate at a site on the scale of decades. These two factors vary over space and time, causing an analogous statistical variability in solar radiation, e.g., [9].

The solar radiation climate at a location provides the levels and trends of the global, diffuse, and direct components over a long period of time (usually equal to or longer than 10 years). Some works have been published in the international literature regarding the solar radiation climate at various locations on Earth; indicative studies are for Barcelona, Spain [10], for Alaska, USA [11], for Central Europe [12], for California, USA [13], for Malawi [9], for Sweden [14], for Thailand [15], for Africa [16], and for Athens, Greece [5]. In Greece no such study has been conducted for the whole country, as there in no organised solar radiation network; the only complete solar platform at the moment is the Actinometric Station of the National Observatory of Athens, established in 1952. Therefore, the present work provides an analysis of the solar radiation climate of Greece for the first time. The diffuse fraction, k_d, i.e., the ratio of the diffuse horizontal to the global horizontal irradiance, H_d/H_g, is used. The direct-beam fraction, k_b, is analogously defined as the ratio of the direct horizontal irradiance to the global horizontal one, H_b/H_g, and is also used in the present work.

The explanation of using the above four parameters (H_g, H_d, k_d, k_b) in characterising the solar radiation climate of Greece is the following. The global radiation expresses the overall solar intensity that arrives at the surface of the Earth and corresponds to the total extinction (absorption and scattering) of the solar rays; the diffuse component refers to the scattering of the solar rays in the atmosphere. The diffuse fraction shows the participation of the scattering process to the total extinction of solar radiation during its passage through the atmosphere; therefore, it can be used as a scattering index. In the same way, the direct-beam fraction mostly reflects the participation of the absorption process to the total extinction of the solar light, and it can become synonymous to an absorption index. The latter is a hypothesis, which is shown to be valid in the analysis of the present work. Moreover, the overall attenuation of solar radiation in the Earth's atmosphere is quantified by the so-called atmospheric turbidity factors, such as the Linke, e.g., [17], the Unsworth–Monteith [18], the Schüepp, e.g., [19] or the Ångström coefficients, e.g., [20].

The structure of the paper is as follows. Section 2 details the sites selected, the corresponding data, and the parameters used for analysis. Section 3 presents annual maps as well as the intra-annual and seasonal variation of the parameters under study. Section 4 provides a discussion about the practicability of the results, while Section 5 deploys the main achievements of the study.

2. Materials and Methods

The analysis of this work is based on data included in typical meteorological years (TMYs). A TMY is a set of meteorological and solar radiation parameters with hourly values usually; these values cover a whole year for a given location [21]. Moreover, a TMY consists of a set of (typical meteorological) months selected from individual years integrated into a complete year [21]. In this way, a TMY reflects all of the specific climatic information of the location for the period it has been generated from. The advantage of using a TMY rather than other methods (e.g., averages of the parameters' values involved) is that it contains original values and not manipulated ones (e.g., averaged).

Kambezidis et al. [21] generated TMYs for 33 sites in Greece. The present study adopts these 33 sites, but 10 additional locations have been added in order to cover more efficiently the area of Greece. Table 1 shows all 43 sites (names and geographical coordinates), while Figure 1 depicts them on the map of Greece. For compatibility purposes the TMYs generated for the 33 sites in [21] have not been used here; TMYs for the 43 sites were downloaded from the PV-Geographical Information System (PV-GIS) tool instead [22], using the latest 2007–2016 Surface Solar Radiation Data Set—Heliostat (SARAH) database [23,24]. Nevertheless, it must be noted here that the TMYs thus derived would be more representative if they would have been generated from a reference period longer than 10 years (as is the period 2007–2016) in view of a changing climate worldwide. This is why the World Meteorological Organisation (WMO) recommends that a 30-year period should be used, if possible, for climatic analyses. However, it is believed that the results of this study will not be differentiated much if a period other than the one adopted would be chosen. This is supported by the fact that the qualitative characteristics of the solar radiation climate of Greece would be retained; the absolute values would only be altered.

The PV-GIS database for each of the 43 sites consists, among others, of columns referring to the year, month, day, hour UTC (universal time coordinated), global horizontal irradiance, H_g (in Wm^{-2}), and diffuse horizontal irradiance, H_d (in Wm^{-2}). The UTC hours were converted to LST (local standard time) = UTC + 2 h. Hourly values of k_d were calculated from hourly values of the ratio H_d/H_g. Hourly values of H_b (in Wm^{-2}) were estimated from the expression $H_b = H_g - H_d$. Hourly values of k_b were obtained from hourly values of the ratio H_b/H_g.

Table 1. The 43 sites involved in the study. The names of the locations are given in alphabetical order. The geographical longitude, λ, and the geographical latitude, φ, are in degrees; E = East (of Greenwich meridian), N = North (hemisphere). The transliteration of the Greek names of the sites into Latin ones follows the ELOT 743 standard [25], which is an adaption of the ISO 843 one [26].

Site #	Site Name/Region/Altitude above Sea Level (m)	λ (° E)	φ (° N)
1	Agrinio/Western Greece/25	21.383	38.617
2	Alexandroupoli/Eastern Macedonia and Thrace/3.5	25.933	40.850
3	Anchialos/Thessaly/15.3	22.800	39.067
4	Andravida/Western Greece/15.1	21.283	37.917
5	Araxos/Western Greece/11.7	21.417	38.133
6	Arta/Epirus/96	20.988	39.158
7	Chios/Northern Aegean/4	26.150	38.350
8	Didymoteicho/Eastern Macedonia and Thrace/27	26.496	41.348
9	Edessa/Western Macedonia/321	22.044	40.802
10	Elliniko/Attica/15	23.750	37.900
11	Ioannina/Epirus/484	20.817	39.700
12	Irakleio/Crete/39.3 (also written as Heraklion)	25.183	35.333
13	Kalamata/Peloponnese/11.1	22.000	37.067
14	Kastelli/Crete/335	25.333	35.120
15	Kastelorizo/Southern Aegean/134	29.576	36.142
16	Kastoria/Western Macedonia/660.9	21.283	40.450
17	Kerkyra/Ionian Islands/4 (also known as Corfu)	19.917	39.617
18	Komotini/Eastern Macedonia and Thrace/44	25.407	41.122
19	Kozani/Western Macedonia/625	21.783	40.283
20	Kythira/Attica/166.8	23.017	36.133
21	Lamia/Sterea Ellada/17.4	22.400	38.850
22	Larisa/Thessaly/73.6	22.450	39.650
23	Lesvos/Northern Aegean/4.8	26.600	39.067
24	Limnos/Northern Aegean/4.6	25.233	39.917
25	Methoni/Peloponnese/52.4	21.700	36.833
26	Mikra/Central Macedonia/4.8	22.967	40.517
27	Milos/Southern Aegean/5	24.475	36.697
28	Naxos/Southern Aegean/9.8	25.533	37.100
29	Orestiada/Eastern Macedonia and Thrace/41	26.531	41.501
30	Rodos/Southern Aegean/11.5 (also written as Rhodes)	28.117	36.400
31	Samos/Northern Aegean/7.3	26.917	37.700
32	Serres/Central Macedonia/34.5	23.567	41.083
33	Siteia/Crete/115.6	26.100	35.120
34	Skyros/Sterea Ellada/17.9	24.550	38.900
35	Souda/Crete/140	21.117	35.550
36	Spata/Attica/67	23.917	37.967
37	Tanagra/Sterea Ellada/139	23.550	38.317
38	Thira/Southern Aegean/36.5	25.433	36.417
39	Thiva/Sterea Ellada/189	23.320	38.322
40	Trikala/Thessaly/114	21.768	39.556
41	Tripoli/Peloponnese/652	22.400	37.533
42	Xanthi/Eastern Macedonia and Thrace/83	24.886	41.130
43	Zakynthos/Ionian Islands/7.9 (also known as Zante)	20.900	37.783

Kambezidis et al. [27] derived a mathematical methodology for determining the upper and lower k_d limits that classify the sky into clear, intermediate and overcast. The methodology was applied to 14 sites around the world. The main result of that work was that universal upper, k_{du}, and lower, k_{dl}, limits may be used, i.e., 0.78 and 0.26, respectively. Therefore, values of k_d in the ranges $0 < k_d \leq k_{dl} = 0.26$ and $0 < k_d \leq 1$ were considered in the present study as they correspond to clear- and all-sky conditions, respectively. Seasonal mean and monthly mean H_g, H_d, k_d, and k_b values were estimated.

Figure 1. Distribution of the 43 sites across Greece. The numbers refer to those in column 1, Table 1. N. = North; S. = South; C. = Central; W. = West; E. = East.

3. Results

3.1. Annual Mean Values

Figure 2 shows the distribution of H_g, H_d, k_d, and k_b for clear- (Figure 2a,c,e,g) and all- (Figure 2b,d,f,h) sky conditions over Greece. Interesting features appear and are commented upon below.

(a)

(b)
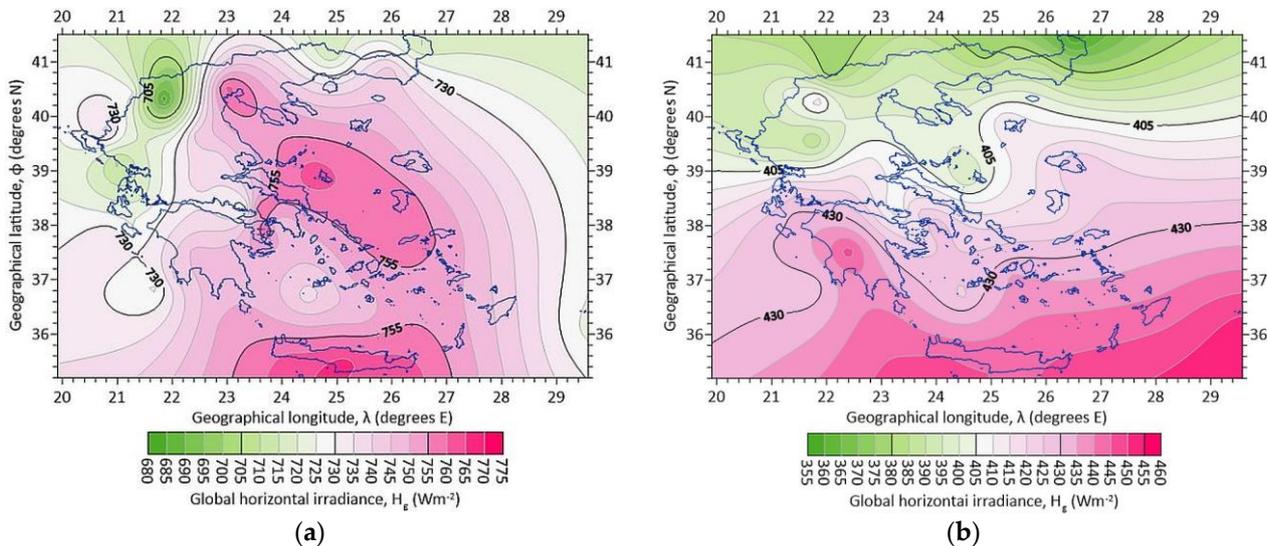
Figure 2. *Cont.*
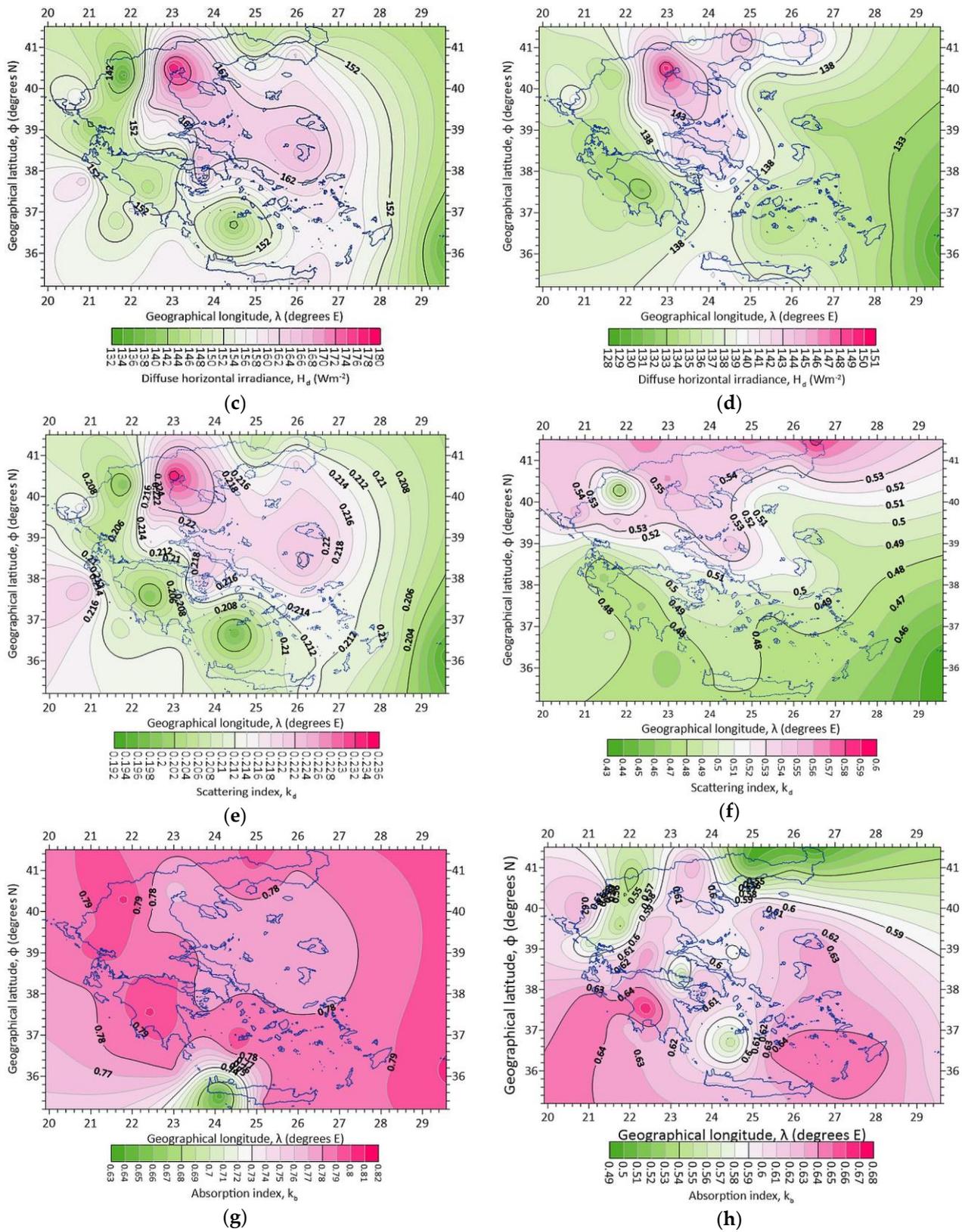
Figure 2. Mean annual (**a**) H_g, (**c**) H_d, (**e**) k_d, and (**g**) k_b values for clear-, and annual mean (**b**) H_g, (**d**) H_d, (**f**) k_d, and (**h**) k_b values for all-sky conditions over Greece.

Under clear skies (Figure 2a), higher H_g values (i.e., $\approx$755 Wm^{-2}) occur in northern Greece (Thessaloniki area), over most of the Aegean and all over Crete. On the contrary,

lower H_g values (i.e., ≈705–730 Wm^{-2}) exist over northwestern Greece (Epirus and most parts of western Macedonia). These observations lead to the conclusion that the total extinction of solar radiation by atmospheric constituents (both natural and additive aerosols such as desert dust, forest fires, and volcanic emissions) is at a minimum over the Aegean region and Crete. This is, of course, a coarse conclusion as one has to take into account the topography and the climatology of each of the 43 sites in the estimation of the solar radiation reaching the ground. Nevertheless, though the altitude of a site plays dominant role in the attenuation level of solar radiation, no clear conclusion seems to be extracted from Figure 3 as regards the 43 sites. Moreover, it is seen that there is great variation in the H_g levels (i.e., ≈662–702 Wm^{-2}) even near the ground level. This may be attributed to both the latitudinal differences among these sites with z < 25 m and to the variable atmospheric turbidity levels over Greece, as depicted in Figures 12 and 13 of [17]. On the other hand, similar H_g levels appear at higher altitudes in comparison to those close to the ground. Figure 3 depicts the influence of both the topography (altitude, terrain) and climatology (geographical latitude) of the sites on solar radiation. In relation to the attenuation of the solar radiation due to the scattering mechanism, Figure 2c shows that this mechanism is stronger over the Aegean Sea (i.e., ≈162 Wm^{-2}) and weaker over the Ionian Sea and western Greece (Epirus, Peloponnese, i.e., ≈140 Wm^{-2}). In Figure 2e the distribution of k_d over Greece is shown; it is seen that the k_d pattern resembles that of H_d and it is, therefore, dominated by it. This means that the clear-sky scattering mechanism is dominant over the absorption one over the Aegean and Thessaloniki area, a conclusion that may be interpreted as the near absence of absorbing substances over these regions. Indeed, the winds in the eastern part of Greece dominate in the NE–SW direction and are generally stronger than those in the western part, thus providing a cleansing effect over the Aegean [28–30]. From the distribution of the absorption index over Greece shown in Figure 2g, it is found that k_b dominates over k_d under clear skies.
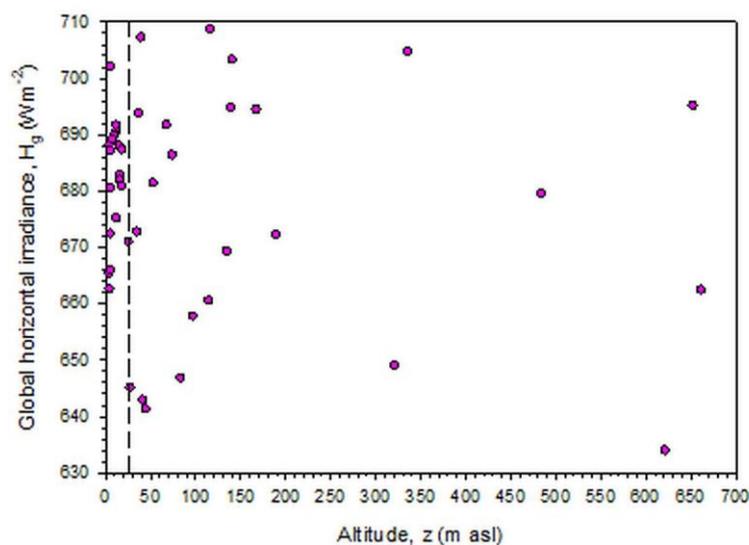
Figure 3. Variation of the annual mean H_g values at the 43 sites under clear-sky conditions as a function of their altitude, z (in m asl; asl = above sea level). It is interesting to observe the great variation in the H_g values (between ≈662 and ≈702 Wm^{-2}) at sites with altitude even lower than 25 m asl (to the left of the vertical black dashed line).

Kambezidis and Psiloglou [17] studied the atmospheric turbidity over Greece by using the Linke turbidity factor, T_L, and the Unsworth–Monteith turbidity coefficient, T_{UM}. They prepared maps of annual mean TL (their Figure 12) and TUM (their Figure 13) values for clear- and all-sky conditions, analogous to Figure 2a,b of the present work. Their distinction of clear skies was made by using the modified clearness index, k'_t [31], in the range $0.65 < k'_t \leq 1$, instead of k_d as in the present work. Another difference is the use of the

33 TMYs derived in [21], while the present study used the PV-GIS TMYs. Therefore, a difference may be found in comparing the H_g-clear-sky map with the T_L-clear-sky (T_{UM}-clear-sky) map. Indeed, T_L and T_{UM} show higher values over the southern Ionian Sea and northern Aegean Sea, while H_g presents higher values over the Aegean and Crete regions. On the contrary, there is a better agreement between the H_d-clear-sky map (Figure 2c) with the T_L and T_{UM} ones. Higher (lower) values of H_d (T_L, T_{UM}) are found over the northern Aegean Sea, and lower (higher) values are found over most of the remaining territory of Greece. This agreement is reasonable, as the H_d solar component clearly addresses the turbidity issue (likewise the T_L and T_{UM} factors) in terms of scattering.

Under all-sky conditions, the H_g pattern (Figure 2b) seems to be much simpler than that for clear skies; the Greek territory is now split into two halves, one in the north and another in the south, with a dividing line at the geographical latitude of about 39° N. This is quite logical, as northern Greece has more cloudiness during the year than the southern part; similar results have been obtained in ([32], Figure 5a) and in ([33], Figure 1i). Cloudiness also dominates the k_d pattern, as expected (Figure 2f, present work), and largely resembles that of H_g. The H_d pattern is similar to that for clear skies; in the case of cloudiness, the maximum over the Aegean is constrained to the northern part of the country (Figure 2d). As far as the absorption index is concerned (Figure 2h), this shows an exactly opposite pattern to that of k_d in Figure 2f. It is notable to observe that the dividing line between these two distinct patterns is again the geographical latitude of 39° N.

In terms of the T_L and T_{UM} values from [17], the H_g pattern is now compatible with that for the two turbidity factors, because in the case of all skies there is no preference in the k_d (k'_t in [17]) values used. Therefore, the main outcome of this section is the right choice of the atmospheric index; k_d (or k'_d, similar to k'_t) refers to the scattering mechanism and k_b to the absorption effect, while the clearness index, k_t (or k'_t), refers to the total (absorption and scattering) extinction of the solar rays.

3.2. Monthly Mean Values

Figure 4 shows the intra-annual distribution of H_g, H_d, k_d, and k_b for clear- (Figure 4a,c,e,g) and all- (Figure 4b,d,f,h) sky conditions over Greece.

Under clear skies, H_g presents a rather broad maximum during the months of May–July. Since the monthly H_g values are averages over all sites, the graph in Figure 4a shows the mean situation over Greece. The broad maximum in the mentioned months may, therefore, be attributed to the (northeasterly) Etesian winds (etesian = annual) that blow every year over the Aegean from May through all summer. It seems that this natural phenomenon is dominant as a cleansing weather system in the eastern part of Greece. Indeed, Figure 2a verifies this (i.e., the high annual H_g values, $\approx$850 Wm^{-2}) over the Aegean. In the case of H_d (Figure 4c), this parameter presents two main maxima, one in April (178 Wm^{-2}) and another in August (168 Wm^{-2}). The two maxima in the figure are in complete agreement with the higher atmospheric turbidity over Greece in these two months (see Figure 10—lower right for TL and Figure 11—lower right for T_{UM}, both in [17]). As far as k_d is concerned, Figure 4e shows that this parameter experiences lower values during summer ($\approx$0.21), meaning a minimum contribution of the scattering particles to the total extinction of the solar rays in the Earth's atmosphere. Indeed, a minimum scattering effect on solar radiation in the summer has been confirmed by other researchers, too. Adamopoulos et al. [34] have estimated a minimum Ångström exponent, α, in the VIS spectrum over Athens equal to 0.69, a value that implies coarser (and more scattering) particles than in the other three seasons. Additionally, Dumka et al. [35] reported a mean value of 0.55 for the scattering Ångström exponent, SAE, over the central Indian Himalayas in the same season. SAE values lower than 1 characterise large scattering particles [36]. As far as k_b is concerned for Greece, rather constant values dominate all over the year with a slight maximum in summer (June, July, Figure 4g, $\approx$0.79). This confirms the k_b pattern in Figure 2g.
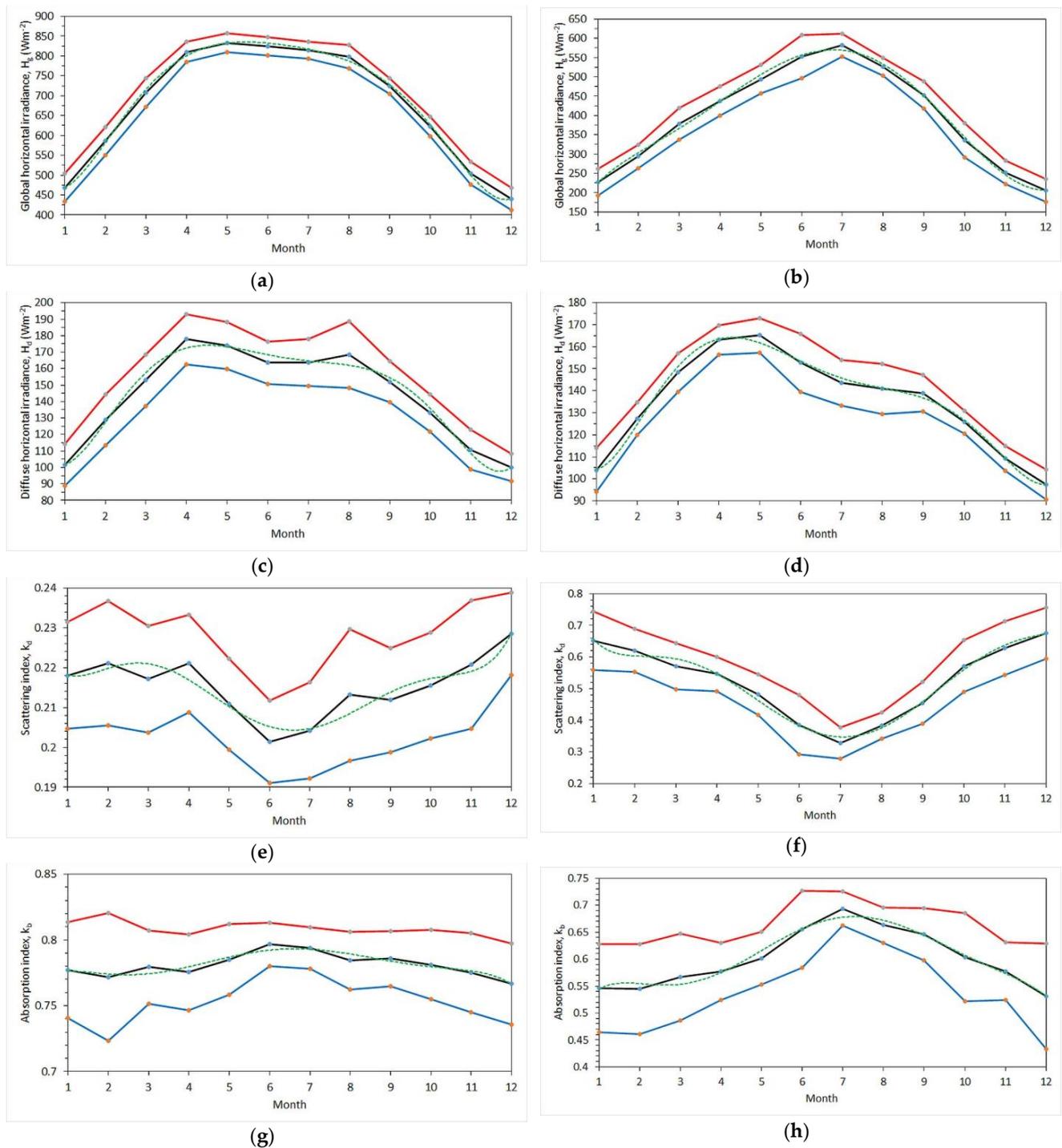
Figure 4. Monthly mean (**a**) H_g, (**c**) H_d, (**e**) k_d, and (**g**) k_b values under clear-, and monthly mean (**b**) H_g, (**d**) H_d, (**f**) k_d, and (**h**) k_b values under all-sky conditions over Greece. The values are averages over all 43 sites. The black lines are the means, and the red and blue curves are the mean + 1σ and mean − 1σ, respectively (σ = standard deviation), while the green dotted lines represent the best-fit curves to the mean values. The months are in sequence of January (1) to December (12).

Under all-sky conditions, H_g (Figure 4b) presents the expected variation of solar radiation with higher values in the summer (here in July, 582 Wm^{-2}). The diffuse solar radiation, though, obtains higher values in springtime (April, May, Figure 4d, ≈165 Wm^{-2}) due to the commencement of desert-dust arrival from northern Africa over Greece, mixed with scattered clouds present in this season; in addition, higher H_d levels are found in late summer (September, ≈139 Wm^{-2}) because of the presence of desert-dust episodes

that are more frequent in spring and extended summer [37]. The intra-annual variation of k_d (Figure 4f) shows a clear minimum in the summer (June, July, $\approx$0.38) because of much lower cloudiness in the sky of Greece in comparison with that in the other three seasons. On the contrary, the k_b index shows an exactly opposite behavior (July, Figure 4h, $\approx$0.69) to k_d, in agreement with the abovementioned behaviour of these two indices.

Figure 4 shows the monthly mean values (black lines) together with the $\pm$95% confidence interval (red and blue lines). The green dotted lines are graphical representation of the regression equations in Table 2 that fit the mean curves best. It is worth observing that all regression lines lie within the $\pm$95% confidence band. R^2 is very close to 1 in almost all cases, except for the clear-sky cases of the k_d and k_b indices. This at-first-glance awkward result occurs because of the great variation of the scattering and absorption mechanisms on clear-sky days. In such situations atmospheric turbulence varies remarkably over space and time (see the complicated patterns in the month–hour Linke- and Unsworth–Monteith turbidity parameter graphs in Figures 6 and 7, respectively, both in [17]). This variability is due to the absence of rain, which is catalytic in the wash-out and removal mechanisms of atmospheric aerosols in the atmosphere.

Table 2. Estimation of the monthly mean values of H_g, H_d, k_d, and k_b, which are averages over all 43 sites; t is month (1 for January, ... , 12 for December). R^2 is the coefficient of determination. Regression polynomials of the 6th order were chosen as giving the highest possible R^2 values.

Parameter	Regression Equation
H_g, clear skies	$H_g = 0.020 \cdot t^6 - 0.760 \cdot t^5 + 11.342 \cdot t^4 - 82.338 \cdot t^3 + 282.550 \cdot t^2 - 304.810 \cdot t + 562.620$ $R^2 = 0.998$
H_g, all skies	$H_g = -0.005 \cdot t^6 + 0.226 \cdot t^5 - 3.927 \cdot t^4 + 29.859 \cdot t^3 - 107.730 \cdot t^2 + 244.860 \cdot t + 61.800$ $R^2 = 0.996$
H_d, clear skies	$H_d = 0.007 \cdot t^6 - 0.262 \cdot t^5 + 3.870 \cdot t^4 - 27.435 \cdot t^3 + 91.751 \cdot t^2 - 107.980 \cdot t + 141.700$ $R^2 = 0.984$
H_d, all skies	$H_d = 0.005 \cdot t^6 - 0.203 \cdot t^5 + 3.148 \cdot t^4 - 23.284 \cdot t^3 + 80.597 \cdot t^2 - 99.505 \cdot t + 143.740$ $R^2 = 0.993$
k_d, clear skies	$k_d = 0.000003 \cdot t^6 - 0.0001 \cdot t^5 + 0.0014 \cdot t^4 - 0.0093 \cdot t^3 + 0.0286 \cdot t^2 - 0.0371 \cdot t + 0.2347$ $R^2 = 0.874$
k_d, all skies	$k_d = 0.00002 \cdot t^6 - 0.0008 \cdot t^5 + 0.0128 \cdot t^4 - 0.0970 \cdot t^3 + 0.3487 \cdot t^2 - 0.5883 \cdot t + 0.9802$ $R^2 = 0.987$
k_b, clear skies	$k_b = -0.000002 \cdot t^6 + 0.00008 \cdot t^5 - 0.0011 \cdot t^4 + 0.0070 \cdot t^3 - 0.0195 \cdot t^2 + 0.0213 \cdot t + 0.7688$ $R^2 = 0.875$
k_b, all skies	$k_b = -0.00001 \cdot t^6 + 0.0004 \cdot t^5 - 0.0062 \cdot t^4 + 0.0453 \cdot t^3 - 0.1559 \cdot t^2 + 0.2419 \cdot t + 0.4185$ $R^2 = 0.972$

3.3. Seasonal Mean Values

Figure 5 shows the seasonal variation of H_g, H_d, k_d, and k_b for clear-(Figure 5a,c,e,g) and all- (Figure 5b,d,f,h) sky conditions over Greece.

Under clear skies, the average summer value of $H_g \approx 813$ Wm^{-2} (Figure 5a) is slightly higher and the average summer value of $H_d \approx 165$ Wm^{-2} (Figure 5c), slightly less than that of spring ($\approx$784 Wm^{-2} and $\approx$168 Wm^{-2}, respectively). On the contrary, the summer k_d value is the lowest among all seasons ($\approx$0.37), a finding that implies least scattering of the solar light over Greece in summertime; this gives way to high k_b values in this season ($\approx$0.79), as expected from the opposite behaviour of these two parameters.

Under all-sky conditions, the average summer H_g level is the highest among all seasons ($\approx$554 Wm^{-2}), as expected, while the H_d one ($\approx$146 Wm^{-2}) is less than that for spring ($\approx$159 Wm^{-2}); the latter implies a greater contribution from the scattering mechanism in the atmosphere during spring than in the summer. Indeed, this conclusion is in agreement with the higher H_d ($\approx$159 Wm^{-2}) and k_d ($\approx$0.53) values in the spring months (April, May, Figure 5d,f) than in the summer months ($\approx$146 Wm^{-2} and $\approx$0.37, respectively). The absorption index shows maximum values in summer ($\approx$0.67, Figure 5h).
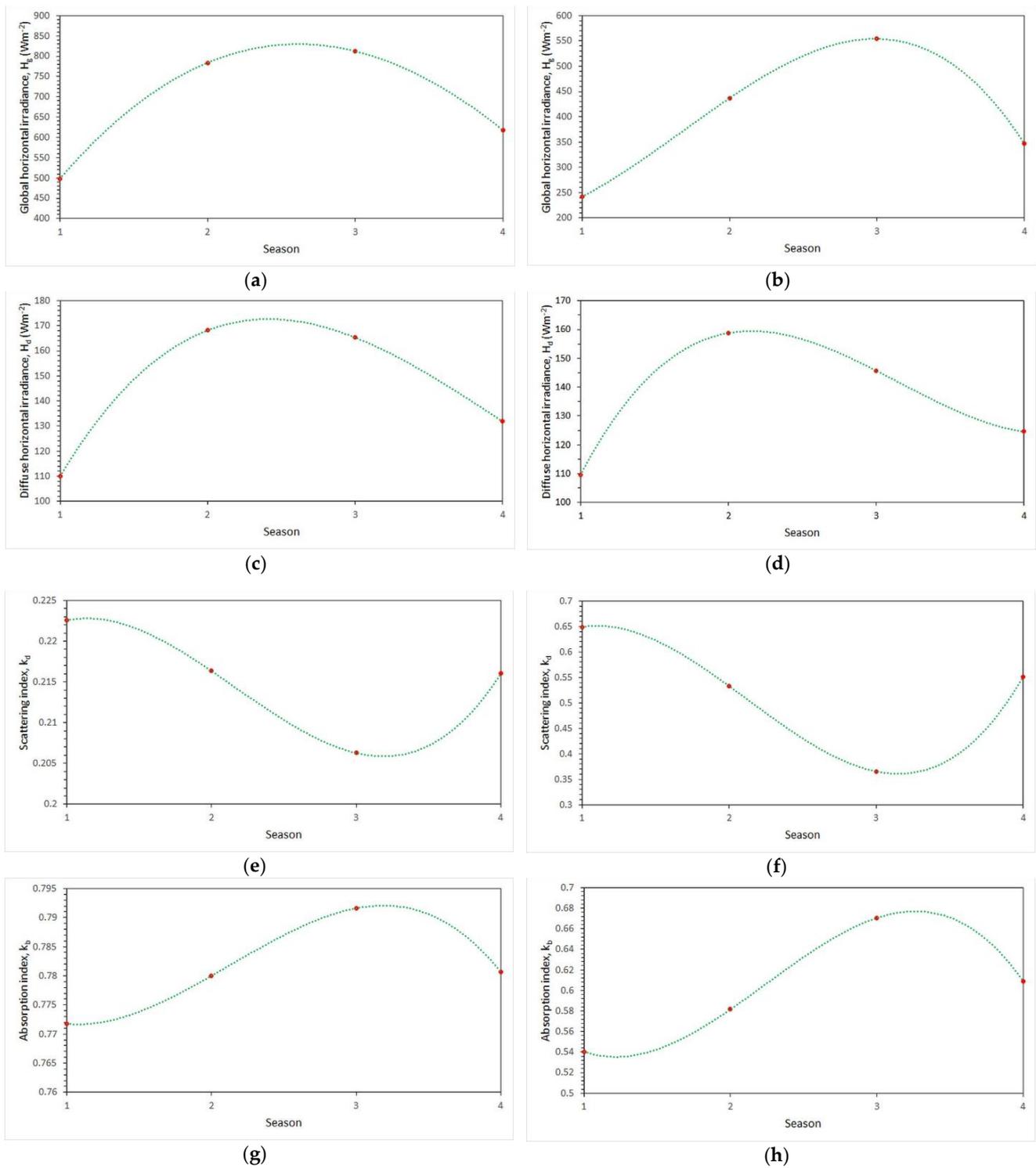
Figure 5. Seasonal mean (**a**) H_g, (**c**) H_d, (**e**) k_d, and (**g**) k_b values under clear skies, and (**b**) H_g, (**d**) H_d, (**f**) k_d, and (**h**) k_b values under all skies over Greece. The values are averages over all 43 sites. The green dotted lines represent the best-fit curves to the seasonal mean values. The seasons are in the sequence of winter (1) to autumn (4); winter = December, January, February; spring = March, April, May; summer = June, July, August; autumn = September, October, November.

For both cases of clear and all skies, third-order regression equations have been derived that best fit the seasonal mean values of H_g, H_d, k_d, and k_b. Their expressions are given in Table 3.

Table 3. Estimation of the seasonal mean values of H_g, H_d, and k_d, which are averages over all 43 sites; t is season (1 for winter, . . . , 4 for autumn). R^2 is the coefficient of determination. Regression polynomials of the 3rd order were chosen as giving the highest possible R^2 values.

Parameter	Regression Equation
H_g, clear skies	$H_g = 5.556 \cdot t^3 - 161.920 \cdot t^2 + 732.780 \cdot t - 78.504$, $R^2 = 1$
H_g, all skies	$H_g = -41.229 \cdot t^3 + 208.770 \cdot t^2 - 143.150 \cdot t + 217.880$, $R^2 = 1$
H_d, clear skies	$H_d = 5.069 \cdot t^3 - 60.891 \cdot t^2 + 205.260 \cdot t - 39.339$, $R^2 = 1$
H_d, all skies	$H_d = 9.010 \cdot t^3 - 85.160 \cdot t^2 + 241.590 \cdot t - 55.834$, $R^2 = 1$
k_d, clear skies	$k_d = 0.004 \cdot t^3 - 0.026 \cdot t^2 + 0.043 \cdot t + 0.201$, $R^2 = 1$
k_d, all skies	$k_d = 0.067 \cdot t^3 - 0.430 \cdot t^2 + 0.701 \cdot t + 0.310$, $R^2 = 1$
k_b, clear skies	$k_b = -0.004 \cdot t^3 + 0.028 \cdot t^2 - 0.045 \cdot t + 0.793$, $R^2 = 1$
k_b, all skies	$k_b = -0.033 \cdot t^3 + 0.222 \cdot t^2 - 0.393 \cdot t + 0.745$, $R^2 = 1$

3.4. Direct Solar Radiation

In order to find any relationship between any of the three solar radiation components with k_d, graphs of their annual mean values were prepared. Scatter-plot graphs of H_g–k_d, H_d–k_d for both clear and all skies, and for H_b–k_d under clear-sky conditions did not show any specific pattern; therefore, they are not presented here. The only meaningful pattern was for the scatter plot of H_b–k_d under all-sky conditions, which is presented in Figure 6. It is interesting to observe that all sites are included in the prediction band, while very few lie within the confidence interval.
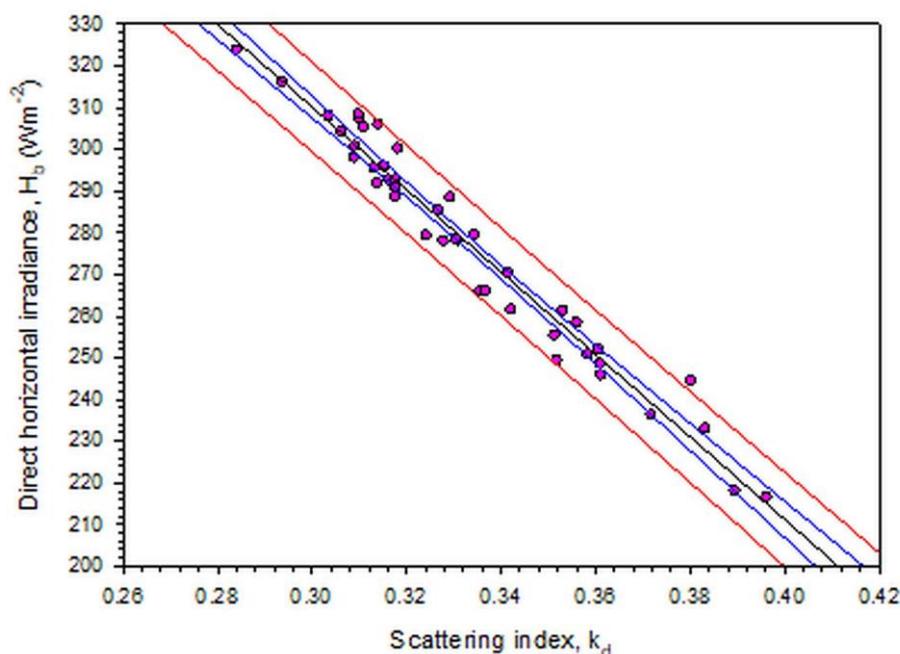
Figure 6. Scatter plot of the annual mean values of H_b for the 43 sites as function of their k_d under all-sky conditions. The black line is a linear fit to the data points expressed by the equation $H_b = -988.799 \cdot k_d + 606.766$ with $R^2 = 0.963$. The blue band represents the $\pm 95\%$ confidence interval, and the red one the $\pm 95\%$ prediction interval.

The confidence interval shows the likely range of the H_b–k_d data pairs to be associated with the fitted regression line; in the 95% case it is anticipated that the regression line passes through each band (i.e., the H_b–k_d value $\pm 1\sigma$), and this happens for up to 95% of the data population. On the contrary, the prediction interval is related to the regression line that passes through the individual ranges of new (future) data pairs; in the 95% case this should occur for up to 95% of new (future) values. The definition of the two intervals can be applied and interpreted in the case of Figure 6 as follows. The regression line loosely

represents the H_b–k_d function, but it is anticipated that this regression equation will be significant (be more confident) in representing new (future) data pairs. The word "future" has the meaning of a changing global climate.

Another interesting feature from Figure 6 is the negative linear dependence of H_b on k_d. If one assumes H_g to be constant in the ratio H_d/H_g, then an increase in H_d (i.e., increase in k_d) results in a decrease in H_b because of the linear relationships $H_g = H_d + H_b$ or $k_d = 1 - H_b/H_g$ (if both sides of the former equation are divided by H_g, the ratio H_d/H_g is replaced with k_d, and the equation is solved for k_d).

3.5. Dependence of H_g on k_d or on φ

Upon investigating the dependence of H_g on k_d or on φ, Figures 7 and 8 were derived. Figure 7 shows a plot of the annual mean H_g values versus the annual mean k_d ones, while Figure 8 presents a scatter plot of the annual mean H_g values versus φ for all 43 sites. Both scatter plots are fitted by linear regression lines from which the annual global horizontal irradiance can be estimated for a known value of k_d or φ. The confidence and prediction intervals are shown and have the same meaning with those in Figure 6.
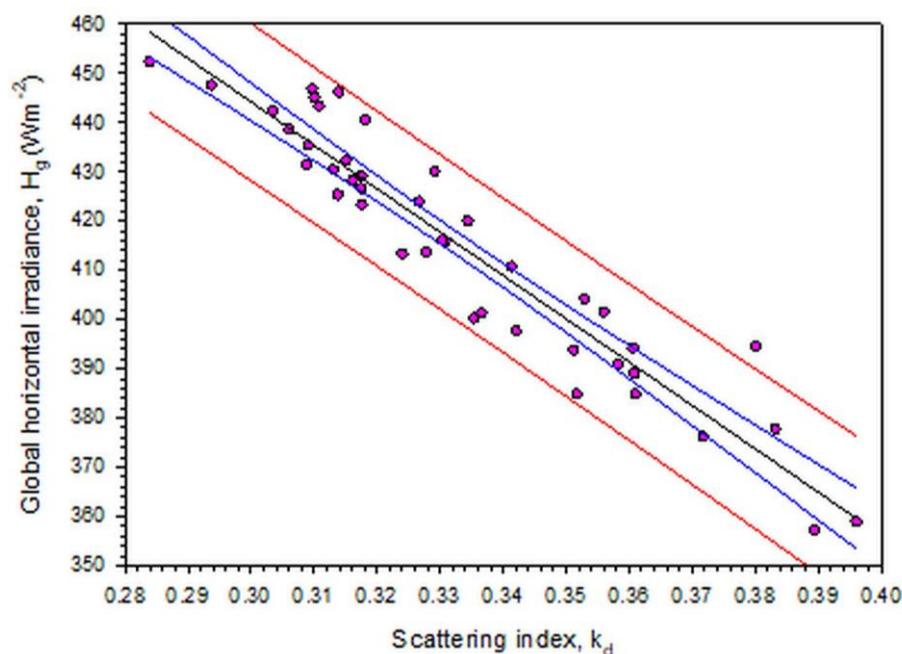
Figure 7. Scatter plot of the annual mean values of H_g for the 43 sites as function of their diffuse fraction, k_d, under all-sky conditions. The black solid line is a linear fit to the data points expressed by the equation $H_g = -880.811 \cdot k_d + 708.462$ with $R^2 = 0.904$. The blue band represents the $\pm 95\%$ confidence interval, and the red one the $\pm 95\%$ prediction interval.
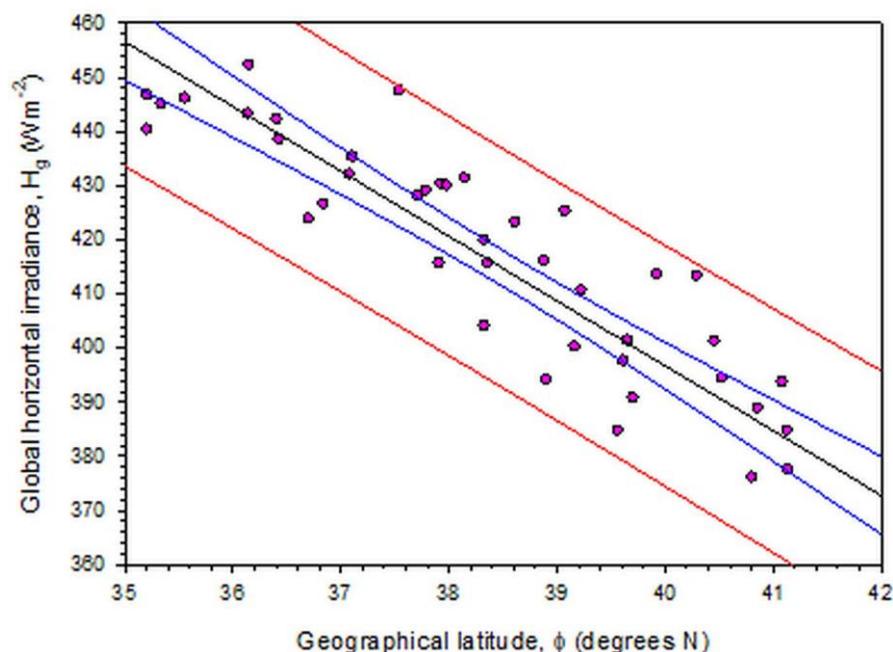
Figure 8. Scatter plot of the annual mean values of H_g for the 43 sites as function of their geographical latitude, φ, under all-sky conditions. The black solid line is a linear fit to the data points expressed by the equation $H_g = -11.968 \cdot \varphi + 875.431$ with $R^2 = 0.809$. The blue band represents the $\pm 95\%$ confidence interval, and the red one the $\pm 95\%$ prediction interval.

3.6. Extinction of Solar Radiation over Greece

In the previous sections the scattering process over Greece was examined in terms of the diffuse fraction (or scattering index), k_d. In the same way, the absorption of solar radiation can be expressed by the direct-beam fraction (or absorption index), $k_b = H_b/H_g$, as mentioned in Section 2. By replacing k_d and k_b with H_d/H_g and H_b/H_g, respectively, in the basic equation $H_g = H_d + H_b$, it is found that $k_d + k_b = 1$. This equation says that the scattering and absorption effects (if reflections in the atmosphere are omitted) are summed up to 1 (i.e., to the total extinction of solar rays). Figure 9 shows the annual mean values of k_d, and k_b over the 43 sites in Greece under clear (Figure 9a) and all (Figure 9b) skies. It is clearly seen that the absorption mechanism is always stronger over Greece than the scattering one, i.e., $k_b \approx 4\, k_d$, and $k_b \approx 2\, k_d$, under clear- and all-sky conditions, respectively.

It is quite interesting to observe that both extinction indices are constant all over Greece under clear-sky conditions. This implies a uniformity of the scattering and absorbing particles over the country. In clear weather, the extinction of solar light is due to the atmospheric constituents (omitting reflections from the ground). The extinction comes from atmospheric particles that scatter (nitrogen, oxygen, desert dust) and/or absorb (carbon dioxide, water vapour, ozone) solar light. The two attenuating mechanisms of solar radiation over Greece are depicted in Figure 9a. The dominance of absorption over scattering under clear skies indicated in Figure 2g is also confirmed in Figure 9.

Under all-sky conditions, the scatterers/absorbers seem to increase/decrease their effect with geographical latitude. This occurs because the extra particles in the atmosphere are now the clouds that scatter solar light. Therefore, as φ increases from $35°$ N to $42°$ N the probability of cloudiness (both cloud cover and clouds type) becomes higher. These causes increase the scattering of solar radiation and, thus, a decrease in absorption occurs because of the basic equation $k_d + k_b = 1$; this equation is verified if the values of k_d and k_b for any $32° < \varphi < 42°$ are added along the best-fit lines in Figure 9a or Figure 9b. Figure 9b depicts the two attenuating mechanisms of solar radiation over Greece for all-sky conditions.
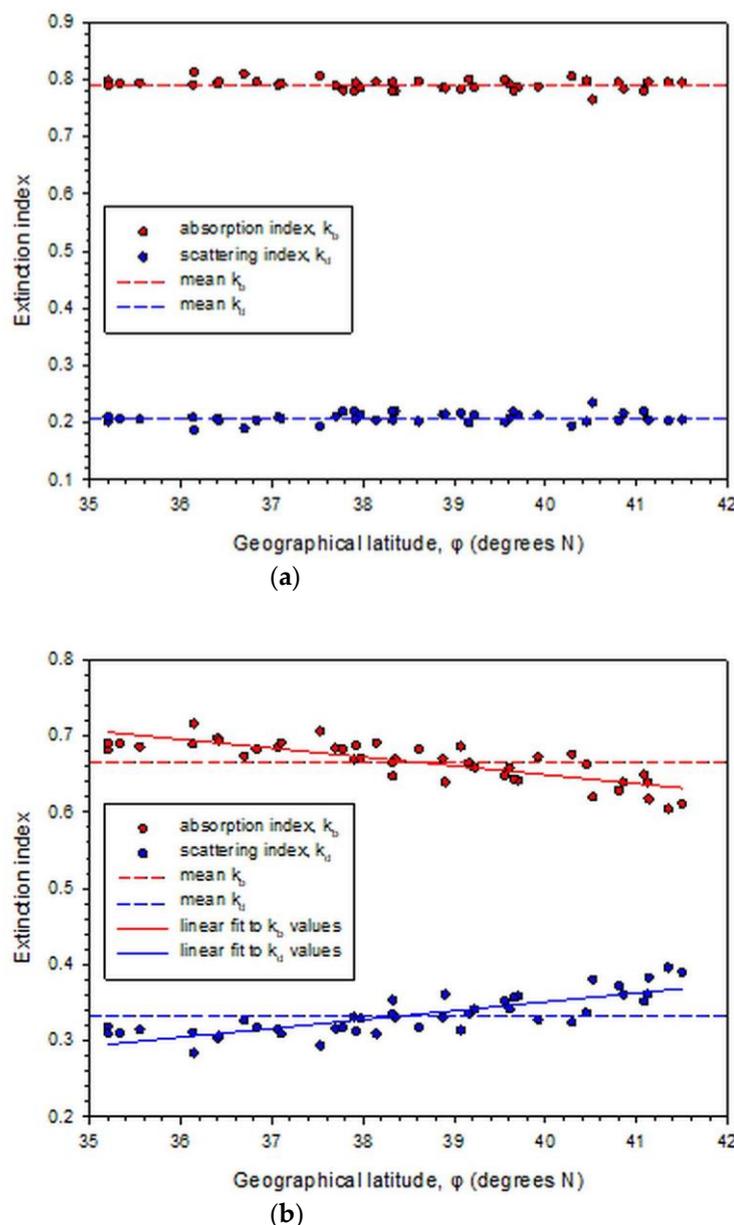
Figure 9. Scatter plots of the annual mean values of the extinction coefficient for the 43 sites as function of their geographical latitude, φ, under (**a**) clear-, and (**b**) all-sky conditions. The horizontal blue and red dashed lines represent the average values of k_d and k_b, respectively. The blue and red solid lines are linear fits to the k_d and k_b data, respectively, expressed by the equations $k_d = 0.0116\ \varphi - 0.1132$ with $R^2 = 0.6532$ and $k_b = -0.0116\ \varphi + 1.1132$ with $R^2 = 0.6532$.

Bai and Zong [38], in an effort to develop a solar radiation model for the location of Qianyanzhou in China to estimate H_g as a sum of absorbing and scattering losses of H_g in the atmosphere, observed that: (i) the absorbing losses (expressed by k_b in the present study) were higher in spring under clear- and all-sky conditions; (ii) the scattering losses (expressed by k_d in their publication and in the present work) were higher in spring and winter under clear skies (in agreement with Figure 5e of the present study) and higher in spring and summer under all skies (not compared well with Figure 5f in the present study; this disagreement may be due to variations in cloudiness during the year between Greece and China); (iii) the extinction of H_g was dominated by absorption losses in all seasons (in agreement with Figure 9 of the present study). The reason that the results in the mentioned study are not in full agreement with those of the present work is due

to the different meteorological patterns occurring year-round over Greece and China. Nevertheless, the fact that some of these results were found to agree between each other provides a basic background for the similar behaviour of the scattering and absorption mechanisms worldwide.

Figure 10 shows the linear relationship between k_b and k_d under all-sky conditions. It is observed that the equation of the fitted line verifies the basic equation $k_b + k_d = 1$.
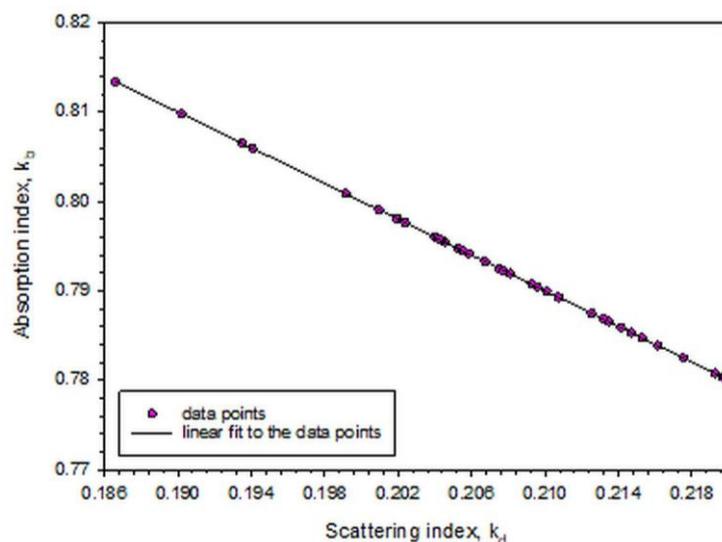
Figure 10. Scatter plot of the annual mean values of k_b (absorption) versus the annual mean values of k_d (scattering) for the 43 sites under all-sky conditions. The black solid line is the linear fit to the data points expressed by the equation $k_b = -k_d + 1$ with $R^2 = 1$.

3.7. Solar Variability and Solar Radiation over Athens

The National Observatory of Athens operates a unique and complete solar platform (the Actinometric Station of the National Observatory of Athens, ASNOA; 37.97° N, 22.72° E, 107 m asl). Figure 11 shows the variation of the annual mean H_g values from the ASNOA records in the period 1953–2018. The yearly sunspot numbers have also been added in the graph for comparison with solar radiation. The periods of the global dimming and global brightening effects over the Athens area [5,39–41] are also indicated. Interesting pieces of information can be extracted from the graph: (i) the solar radiation recorded at ASNOA does not follow exactly the solar activity (sunspots cycle); (ii) the peaks of solar activity (highest sunspot numbers) do not necessarily coincide with the peaks in solar radiation; (iii) solar radiation has been recently increasing, though the solar activity after 2007 (solar cycle 24) is very low (quiet Sun); (iv) the absence of co-variance between the two data series shows that solar activity has a less significant effect on solar radiation reaching the surface of the Earth in comparison with the effect exerted by atmospheric aerosols. Indeed, the global dimming effect has been attributed to an increase in anthropogenic (air pollution) aerosols mainly over big cities and large industrial estates [42–44].
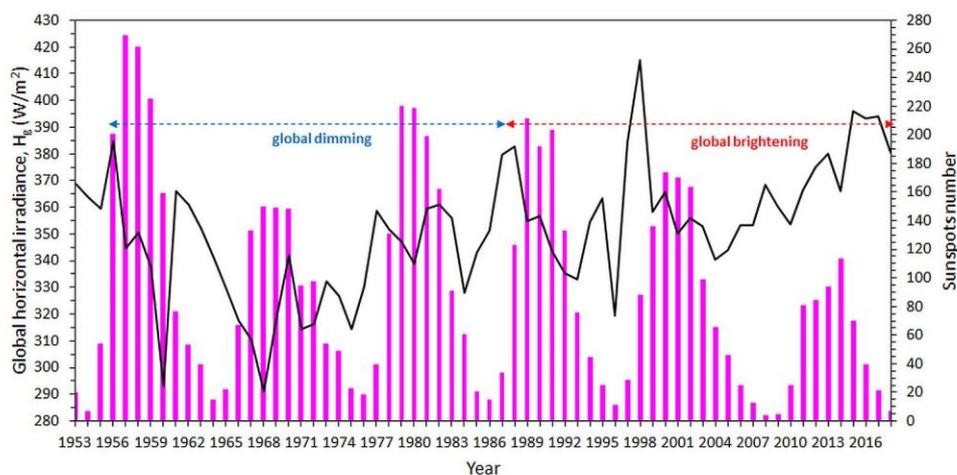
Figure 11. Diachronic variation of the annual mean H_g values (black solid line) and the sunspot number (vertical pink bars) over Athens in the period 1953–2018. The global dimming and brightening effects are indicated by blue and red double-headed arrows, respectively. The solar radiation values come from the ASNOA records, and the sunspot numbers from the Solar Influences Data Analysis Centre, Royal Observatory of Belgium.

4. Discussion

The present work studied the solar radiation climate of Greece. That was done through adopting typical meteorological years for 43 sites in Greece. The use of TMYs in various applications is attracting more and more attention by scientists/users because each TMY contains robust information for the climate at a location; see, e.g., [21,45–47]. The use of TMYs is also attracting attention in solar radiation applications; see, e.g., [48–51].

The present work was the first for Greece in studying the solar radiation climate of the country and among few in the international literature. The knowledge of the solar climate of a region or a country is precious as it dictates the solar availability, i.e., the solar radiation levels expected, and, to a certain extent, it elucidates the climate of the area, because solar radiation is one of the most important parameters comprising local climate. The analysis in the present study was focused on the three solar radiation components based on the TMYs of 43 sites in Greece. Use of the diffuse fraction, k_d, (or else cloudiness index [52]), and the absorption index, k_b, was made. As far as the latter index is concerned, this was the first time that it was introduced in the literature to the author's best knowledge.

The diffuse fraction (the scattering index) shows the weight of the diffusively scattered solar radiation by atmospheric molecules (in clear-sky conditions) and by atmospheric aerosols and clouds combined (under all-sky conditions) over the received global solar radiation on the surface of the Earth; in other words, k_d reflects the attenuation of solar radiation by scattering in the atmosphere. The direct-beam fraction (the absorption index) shows the weight of the attenuated (absorbed) direct solar radiation by atmospheric molecules (under clear skies) or attenuated (absorbed and scattered) by atmospheric aerosols and clouds (under all skies) to the received global solar irradiance on the surface of the Earth. The present study speculated that k_b represents more the absorption of solar radiation than the scattering effect. The assumption proved to be true from solar radiation measurements, as demonstrated in Figures 9 and 10.

From the above, it is concluded that the k_d and k_b indices (and especially the k_b one introduced in the present work) can from now on be used in studies describing the atmospheric scattering and absorption mechanisms, respectively. This conclusion becomes robust because of the evaluation of the basic equation $k_b + k_d = 1$.

5. Conclusions

In view of the above, the following conclusions can be summarised.

- Under clear skies, higher annual H_g values occur in northern Greece (Thessaloniki area), over most of the Aegean and all over Crete. On the contrary, lower annual H_g values exist over northwestern Greece (Epirus and most parts of western Macedonia). The annual k_d pattern resembles that of H_d. High values of k_b dominate almost all over Greece.
- Under all-sky conditions, the annual H_g pattern is split into two halves, one in the north and another in the south with a dividing line at the latitude of about $39°$ N. The distribution of the annual H_d levels is similar to that for clear skies. The annual k_d pattern resembles much that of H_g, while that for k_b is quite the opposite.
- Under clear skies, the intra-annual H_g levels present a rather broad maximum during the months of May–July. In the case of H_d, this parameter presents two main maxima, one in April and another in August. As far as k_d is concerned, this parameter experiences lower values during the summer. The absorption index shows a rather flat behaviour throughout the year.
- Under all-sky conditions, the monthly mean H_g values are higher in the summer (here in July). The diffuse solar radiation, though, obtains higher values in springtime (April, May). The intra-annual variation of k_d shows a clear minimum in the summer (June, July), whereas k_b obtains maximum values in the summer.
- Under clear skies, the average summer value of H_g is slightly higher and the average summer value of H_d slightly lower than that of spring. The average summer value of k_d is the lowest among all seasons, while that for k_b is the highest. The same conclusions apply in the case of all skies.
- Under all skies, H_g decreases with increasing k_d; the same behaviour exists for increasing φ.
- The k_d and k_b indices reflect the scattering and absorption mechanisms of solar radiation in the atmosphere. The expression $k_d + k_b = 1$ was validated.
- k_d increases and k_b decreases with increasing φ under all-sky conditions.

References

1. Giesen, R.H.; van den Broeke, M.R.; Oerlemans, J.; Andreassen, L.M. Surface energy balance in the ablation zone of Midtdalsbreen, a glacier in Southern Norway: Interannual variability and the effect of clouds. *J. Geophys. Res.* **2008**, *113*, D21111. [CrossRef]
2. Asaf, D.; Rotenberg, E.; Tatarinov, F.; Dicken, U.; Montzka, S.A.; Yakir, D. Ecosystem photosynthesis inferred from measurements of carbonyl sulphide flux. *Nat. Geosci.* **2013**, *6*, 186–190. [CrossRef]
3. Bojinski, S.; Verstraete, M.; Peterson, T.C.; Richter, C.; Simmons, A.; Zemp, M. The concept of essential climate variables in support of climate research, applications, and policy. *Bull. Am. Meteorol. Soc.* **2014**, *95*, 1431–1443. [CrossRef]
4. Kambezidis, H.D. The solar resource. In *Comprehensive Renewable Energy*; Elsevier: Amsterdam, The Netherlands, 2012; Volume 3. [CrossRef]
5. Kambezidis, H.D. The solar radiation climate of athens: Variations and tendencies in the period 1992–2017, the Brightening Era. *Sol. Energy* **2018**, *173*, 328–347. [CrossRef]
6. Forster, P.M. Inference of climate sensitivity from analysis of earth's energy budget. *Annu. Rev. Earth Planet. Sci.* **2016**, *44*, 85–106. [CrossRef]

7.   Haywood, J.; Boucher, O. Estimates of the direct and indirect radiative forcing due to tropospheric aerosols: A review. *Rev. Geophys.* **2000**, *38*, 513–543. [CrossRef]

8.   Puetz, S.J.; Prokoph, A.; Borchardt, G. Evaluating alternatives to the milankovitch theory. *J. Stat. Plan. Inference* **2016**, *170*, 158–165. [CrossRef]

9.   Madhlopa, A. Solar radiation climate in malawi. *Sol. Energy* **2006**, *80*, 1055–1057. [CrossRef]

10.   Jiménez, J.I. Solar radiation statistic in Barcelona, Spain. *Sol. Energy* **1981**, *27*, 271–282. [CrossRef]

11.   Dissing, D.; Wendler, G. Solar radiation climatology of Alaska. *Theor. Appl. Climatol.* **1998**, *61*, 161–175. [CrossRef]

12.   Petrenz, N.; Sommer, M.; Berger, F.H. Long-time global radiation for Central Europe derived from ISCCP Dx data. *Atmos. Chem. Phys.* **2007**, *7*, 5021–5032. [CrossRef]

13.   Nottrott, A.; Kleissl, J. Validation of the NSRDB-SUNY global horizontal irradiance in California. *Sol. Energy* **2010**, *84*, 1816–1827. [CrossRef]

14.   Persson, T. Solar radiation climate in Sweden. *Phys. Chem. Earth* **1999**, *24*, 275–279. [CrossRef]

15.   Exell, R.H.B. The solar radiation climate of Thailand. *Sol. Energy* **1976**, *18*, 349–354. [CrossRef]

16.   Diabaté, L.; Blanc, P.; Wald, L. Solar radiation climate in Africa. *Sol. Energy* **2004**, *76*, 733–744. [CrossRef]

17.   Kambezidis, H.D.; Psiloglou, B.E. Climatology of the Linke and Unsworth-Monteith turbidity parameters for Greece: Introduction to the notion of a typical atmospheric turbidity year. *Appl. Sci.* **2020**, *10*, 4043. [CrossRef]

18.   Unsworth, M.H.; Monteith, J.L. Aerosol and solar radiation in Britain. *Q. J. R. Meteorol. Soc.* **1972**, *98*, 778–797. [CrossRef]

19.   Kambezidis, H.D.; Adamopoulos, A.D.; Zevgolis, D. Determination of Ångström and Schüepp's parameters from ground-based spectral measurements of beam irradiance in the ultraviolet and visible spectrum in Athens, Greece. *Pure Appl. Geophys.* **2001**, *158*, 821–838. [CrossRef]

20.   Janjai, S.; Kumharn, W.; Laksanaboonsong, J. Determination of angstrom's turbidity coefficient over Thailand. *Renew. Energy* **2003**, *28*, 1685–1700. [CrossRef]

21.   Kambezidis, H.D.; Psiloglou, B.E.; Kaskaoutis, D.G.; Karagiannis, D.; Petrinoli, K.; Gavriil, A.; Kavadias, K. Generation of typical meteorological years for 33 locations in Greece: Adaptation to the needs of various applications. *Theor. Appl. Climatol.* **2020**, *141*, 1313–1330. [CrossRef]

22.   Huld, T.; Müller, R.; Gambardella, A. A new solar radiation database for estimating PV performance in Europe and Africa. *Sol. Energy* **2012**, *86*, 1803–1815. [CrossRef]

23.   Urraca, R.; Gracia-Amillo, A.M.; Koubli, E.; Huld, T.; Trentmann, J.; Riihelä, A.; Lindfors, A.V.; Palmer, D.; Gottschalg, R.; Antonanzas-Torres, F. Extensive validation of CM SAF surface radiation products over Europe. *Remote Sens. Environ.* **2017**, *199*, 171–186. [CrossRef] [PubMed]

24.   Urraca, R.; Huld, T.; Gracia-Amillo, A.; Martinez-de-Pison, F.J.; Kaspar, F.; Sanz-Garcia, A. Evaluation of global horizontal irradiance estimates from ERA5 and COSMO-REA6 reanalyses using ground and satellite-based data. *Sol. Energy* **2018**, *164*, 339–354. [CrossRef]

25.   ELOT. *Information and Documentation: Conversion of Greek Characters into Latin Characters. Standard 743*; Multiple. Distributed through American National Standards Institute: Washington, DC, USA, 2001; ICS 01.140.10.

26.   ISO. *Information and Documentation: Conversion of Greek Characters into Latin Characters. Standard 843*; Multiple. Distributed through American National Standards Institute: Washington, DC, USA, 1997; ICS 01.140.10.

27.   Kambezidis, H.D.; Kampezidou, S.I.; Kampezidou, D. Mathematical determination of the upper and lower limits of the diffuse fraction at any site. *Appl. Sci.* **2021**, *11*, 8654. [CrossRef]

28.   Sahsamanoglou, H.S.; Bloutsos, A.A. Cleansing of the atmosphere in the Athens area by means of rainfall and wind. *Energy Build.* **1982**, *4*, 125–128. [CrossRef]

29.   Adamopoulos, A.D.; Kambezidis, H.D.; Zevgolis, D. Total atmospheric transmittance in the UV and VIS spectra in Athens, Greece. *Pure Appl. Geophys.* **2005**, *162*, 409–431. [CrossRef]

30.   Giavis, G.M.; Kambezidis, H.D.; Lykoudis, S.P. Frequency distribution of particulate MATTER (PM10) in urban environments. *Int. J. Environ. Pollut.* **2009**, *36*, 99–109. [CrossRef]

31.   Perez, R.; Ineichen, P.; Seals, R.; Zelenka, A. Making full use of the clearness index for parameterizing hourly insolation conditions. *Sol. Energy* **1990**, *45*, 111–114. [CrossRef]

32.   Katopodis, T.; Markantonis, I.; Politi, N.; Vlachogiannis, D.; Sfetsos, A. High-resolution solar climate atlas for Greece under climate change using the weather research and forecasting (WRF) model. *Atmosphere* **2020**, *11*, 761. [CrossRef]

33.   Ioannidis, E.; Lolis, C.J.; Papadimas, C.D.; Hatzianastassiou, N.; Bartzokas, A. On the intra-annual variation of cloudiness over the Mediterranean region. *Atmos. Res.* **2018**, *208*, 246–256. [CrossRef]

34.   Adamopoulos, A.D.; Kambezidis, H.D.; Kaskaoutis, D.G.; Giavis, G. A study of aerosol particle sizes in the atmosphere of Athens, Greece, retrieved from solar spectral measurements. *Atmos. Res.* **2007**, *86*, 194–206. [CrossRef]

35.   Dumka, U.C.; Kaskaoutis, D.G.; Sagar, R.; Chen, J.; Singh, N.; Tiwari, S. First results from light scattering enhancement factor over central Indian Himalayas during GVAX campaign. *Sci. Total Environ.* **2017**, *605–606*, 124–138. [CrossRef] [PubMed]

36.   Schmeisser, L.; Andrews, E.; Ogren, J.A.; Sheridan, P.; Jefferson, A.; Sharma, S.; Kim, J.E.; Sherman, J.P.; Sorribas, M.; Kalapov, I.; et al. Classifying aerosol type using in situ surface spectral aerosol optical properties. *Atmos. Chem. Phys.* **2017**, *17*, 12097–12120. [CrossRef]

37. Gkikas, A.; Hatzianastassiou, N.; Mihalopoulos, N.; Katsoulis, V.; Kazadzis, S.; Pey, J.; Querol, X.; Torres, O. The regime of intense desert dust episodes in the Mediterranean based on contemporary satellite observations and ground measurements. *Atmos. Chem. Phys.* **2013**, *13*, 12135–12154. [CrossRef]
38. Bai, J.; Zong, X. Global solar radiation transfer and its loss in the atmosphere. *Appl. Sci.* **2021**, *11*, 2651. [CrossRef]
39. Kambezidis, H.D.; Kaskaoutis, D.G.; Kharol, S.K.; Moorthy, K.K.; Satheesh, S.K.; Kalapureddy, M.C.R.; Badarinath, K.V.S.; Sharma, A.R.; Wild, M. Multi-decadal variation of the net downward shortwave radiation over South Asia: The solar dimming effect. *Atmos. Environ.* **2012**, *50*, 360–372. [CrossRef]
40. Nastos, P.T.; Kambezidis, H.D.; Demetriou, D. Solar dimming/brightening within the Mediterranean. In Proceedings of the 13th International Conference on Environmental Science and Technology, Athens, Greece, 5–7 September 2013; Global NEST: Athens, Greece, 2013. ISBN 978-960-7475-51-0.
41. Kambezidis, H.D.; Kaskaoutis, D.G.; Kalliampakos, G.K.; Rashki, A.; Wild, M. The solar dimming/brightening effect over the Mediterranean basin in the period 1979–2012. *J. Atmos. Sol.-Terr. Phys.* **2016**, *150–151*, 31–46. [CrossRef]
42. Gilgen, H.; Wild, M.; Ohmura, A. Means and trends of shortwave irradiance at the surface estimated from global energy balance archive data. *J. Clim.* **1998**, *11*, 2042–2061. [CrossRef]
43. Gilgen, H.; Roesch, A.; Wild, M.; Ohmura, A. Decadal changes in shortwave irradiance at the surface in the period from 1960 to 2000 estimated from global energy balance archive data. *J. Geophys. Res. Atmos.* **2009**, *114*. [CrossRef]
44. Wild, M. Global dimming and brightening: A review. *J. Geophys. Res. Atmos.* **2009**, *114*. [CrossRef]
45. Chan, A.L.S. Generation of typical meteorological years using genetic algorithm for different energy systems. *Renew. Energy* **2016**, *90*, 1–13. [CrossRef]
46. Farah, S.; Saman, W.; Boland, J. Development of robust meteorological year weather data. *Renew. Energy* **2018**, *118*, 343–350. [CrossRef]
47. Janjai, S.; Deeyai, P. Comparison of methods for generating typical meteorological year using meteorological data from a tropical environment. *Appl. Energy* **2009**, *86*, 528–537. [CrossRef]
48. Bre, F.; e Silva Machado, R.M.; Lawrie, L.K.; Crawley, D.B.; Lamberts, R. Assessment of solar radiation data quality in typical meteorological years and its influence on the building performance simulation. *Energy Build.* **2021**, *250*, 111251. [CrossRef]
49. Mosalam Shaltout, M.A.; Tadros, M.T.Y. Typical solar radiation year for egypt. *Renew. Energy* **1994**, *4*, 387–393. [CrossRef]
50. Chang, K.; Zhang, Q. Improvement of the hourly global solar model and solar radiation for air-conditioning design in China. *Renew. Energy* **2019**, *138*, 1232–1238. [CrossRef]
51. Huang, K.T. Identifying a suitable hourly solar diffuse fraction model to generate the typical meteorological year for building energy simulation application. *Renew. Energy* **2020**, *157*, 1102–1115. [CrossRef]
52. Soneye, O.O. Evaluation of clearness index and cloudiness index using measured global solar radiation data: A case study for a tropical climatic region of Nigeria. *Atmosfera* **2021**, *34*, 25–39. [CrossRef]